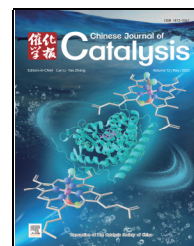


available at [www.sciencedirect.com](http://www.sciencedirect.com)journal homepage: [www.sciencedirect.com/journal/chinese-journal-of-catalysis](http://www.sciencedirect.com/journal/chinese-journal-of-catalysis)

## Article

# Boosting the Volmer step by synergistic coupling of dilute CuRu nanoalloy with Cu/Ru dual single atoms for efficient and CO-tolerant alkaline hydrogen oxidation

Yi Liu <sup>a</sup>, Shuqing Zhou <sup>a</sup>, Chenggong Niu <sup>a</sup>, Tayirjan Taylor Isimjan <sup>b</sup>, Yongfa Zhu <sup>c</sup>,  
Dingsheng Wang <sup>c</sup>, Xiulin Yang <sup>a,\*</sup>, Jieshan Qiu <sup>d,\*</sup>, Bin Wu <sup>e,\*</sup>

<sup>a</sup> Guangxi Key Laboratory of Low Carbon Energy Materials, School of Chemistry and Pharmaceutical Sciences, Guangxi Normal University, Guilin 541004, Guangxi, China

<sup>b</sup> Saudi Arabia Basic Industries Corporation (SABIC) at King Abdullah University of Science and Technology (KAUST), Thuwal 23955-6900, Saudi Arabia

<sup>c</sup> Department of Chemistry, Tsinghua University, Beijing 100084 China

<sup>d</sup> State Key Laboratory of Chemical Resource Engineering, College of Chemical Engineering, Beijing University of Chemical Technology, Beijing 100029, China

<sup>e</sup> School of Materials Science and Engineering, Nanyang Technological University, Singapore 639798, Singapore



## ARTICLE INFO

## Article history:

Received 16 November 2024

Accepted 24 February 2025

Available online 20 May 2025

## Keywords:

Dilute CuRu nanoalloy

N incorporation

Hydrogen oxidation reaction

Synergistic effect

CO-tolerant

## ABSTRACT

Active and poisoning-resistant Ru-based electrocatalysts for the hydrogen oxidation reaction (HOR) are designed and fabricated by integrating Cu/Ru dual single atoms and alloy CuRu nanoparticles (N-(CuRu)<sub>NP+SA</sub>@NC) through a strategy involving weak chemical reduction and ammonia-assisted gas-phase nitridation. The resultant N-(CuRu)<sub>NP+SA</sub>@NC electrocatalysts feature nitrogen atoms coordinated to both Cu and Ru metal atoms via strong N-metal interactions. Density functional theory calculations revealed that alloyed CuRu nanoparticles and monodispersed Cu atoms are vital for altering the electronic configuration of the host Ru elements. This finely tuned structure enhanced the adsorption of H and OH and promoted CO oxidation over the N-(CuRu)<sub>NP+SA</sub>@NC electrocatalyst, resulting in high alkaline HOR activity, as evidenced by the higher exchange current density of 3.74 mA cm<sup>-2</sup> and high mass activity of 3.28 mA μg<sub>Ru</sub><sup>-1</sup>, which are far superior to those of most Ru-based catalysts reported to date. Moreover, the N-(CuRu)<sub>NP+SA</sub>@NC electrocatalysts are resistant to CO poisoning and can be used at a high concentration of 1000 ppm CO with no distinct decay in the activity, in stark contrast to the commercial Pt/C catalyst under the same conditions.

© 2025, Dalian Institute of Chemical Physics, Chinese Academy of Sciences.

Published by Elsevier B.V. All rights reserved.

## 1. Introduction

Hydrogen-oxygen fuel cells (HOFCs) facilitate the conversion of hydrogen into electricity and are considered to be the

cornerstone of the emerging green hydrogen economy [1]. Among HOFCs, alkaline exchange membrane fuel cells (AEMFCs) have attracted widespread attention because they exploit nonprecious metal electrocatalysts to efficiently carry

\* Corresponding author. E-mail: [xlyang@gxnu.edu.cn](mailto:xlyang@gxnu.edu.cn) (X. Yang), [qiujs@mail.buct.edu.cn](mailto:qiujs@mail.buct.edu.cn) (J. Qiu), [bin.wu@ntu.edu.sg](mailto:bin.wu@ntu.edu.sg) (B. Wu).

This work was supported by the National Natural Science Foundation of China (52363028, 21965005), the Natural Science Foundation of Guangxi Province (2021GXNSFAA076001, 2018GXNSFAA294077), the Guangxi Technology Base and Talent Subject (GUIKE AD23023004, GUIKE AD20297039), the National Research Foundation, Singapore, and A\*STAR (Agency for Science, Technology and Research) under its LCER Phase 2 Programme Hydrogen & Emerging Technologies FI, Directed Hydrogen Programme (U2305D4003).

[https://doi.org/10.1016/S1872-2067\(25\)64670-5](https://doi.org/10.1016/S1872-2067(25)64670-5)

out the cathodic oxygen reduction reaction [2,3]. However, the anodic hydrogen oxidation reaction (HOR) in AEMFCs relies heavily on platinum group metals (PGMs) to achieve high performance and also shows significantly slower kinetics at high pH levels [4,5]. Even for state-of-the-art Pt/C catalysts, the HOR kinetics are typically 2–3 orders of magnitude slower in alkaline electrolytes than in acidic electrolytes [6,7]. Consequently, AEMFC catalysts require high PGM loadings to achieve the desired power density. Although PGMs are the most effective catalysts for the alkaline HOR, their limited natural abundance and susceptibility to CO (< 10 ppm) poisoning significantly impede their extensive application [8]. Therefore, development of Pt-free HOR electrocatalysts that show low cost, high performance, and resistance to CO poisoning is necessary to promote the commercialization of AEMFCs.

In the Volmer process, the adsorbed OH\* quickly reacts with adjacent H\* to form H<sub>2</sub>O, making hydrogen binding energy (HBE) and hydroxyl binding energy (OHBE) the critical parameters for alkaline HOR activity [9]. Ruthenium been identified as an ideal alternative to Pt because of its lower cost, superior oxygenophilicity, and H\* adsorption free energy ( $\Delta G_{H^*}$ ) comparable to that of Pt [10]. However, the strong Ru–H bond of the Ru metal severely hampers the rate-determining Volmer step, hindering H<sub>2</sub>O formation [11,12]. To address this issue, researchers have exploited strategies such as alloying, multisite modulation, and single-atom modification to precisely tune the electronic structure of Ru and optimize H\* and OH\* adsorption [13]. Previous studies have suggested that alloying low-electronegativity 3d transition metals (Cu:1.9, Ni: 1.9, Co:1.88) with Ru promotes electron transfer from Ru to the alloying metal, shifting the *d*-band center upward and reducing the  $\Delta G_{H^*}$  value [14,15]. However, excess foreign elements can obscure the active sites and limit their activity [16]. A dilute alloying approach optimizes H<sub>ad</sub> and OH<sub>ad</sub> while preserving most of the Ru active sites and weakening CO adsorption. Additionally, single-atom catalysts (SACs), featuring isolated metal atoms anchored to suitable supports, are promising candidate electrocatalysts because of their ultralow metal content, maximized atom efficiency, and exceptionally high intrinsic activity [17–19]. Due to these attributes, SACs act as high-performance catalysts for various electrochemical reactions [20,21]. The combination of alloying and single-atom modification strategies can synergistically enhance the alkaline HOR activity, stability, and CO poisoning resistance of Ru-based catalysts [22]. Han *et al.* [23] constructed a composite catalyst composed of dilute RuCo alloy nanoparticles and individual Ru and Co atoms that demonstrated remarkable stability and CO tolerance. Heteroatom (N, P, and S) doping is a promising method for modulating the electronic structure of a host material without changing its composition [24].

Based on these insights, we developed a novel electrocatalyst by integrating dilute alloying and single-atom modification to enhance alkaline HOR performance. The resulting catalyst, consisting of dilute CuRu alloy nanoparticles and monodispersed Cu/Ru single atoms (denoted as N-(CuRu)<sub>NP+SA</sub>@NC), demonstrated significantly improved catalytic activity, durability, and resistance to CO poisoning, outperforming the

state-of-the-art Pt/C catalyst. Theoretical calculations revealed that the electronic interaction between Ru and Cu, coupled with effective N incorporation, optimized H\* and OH\* adsorption, and expedited CO oxidation, ultimately facilitating the key Volmer step and increasing CO tolerance. These attractive features indicate that the combination of dilute alloying and single-atom modification used in this study is a promising strategy for the development of HOR electrocatalysts for fuel cells.

## 2. Experimental

### 2.1. Synthesis of N-doped hollow mesoporous carbon spheres (HMCS)

The HMCS were prepared via stirring reaction, high-annealing and alkali-etching methods based on our previous report [25]. Specifically, 5 mL of TEOS and 500 mg of 3-hydroxytyramine hydrochloride were quickly added to a solution containing 100 mL of ethanol, 30 mL of deionized water, and 5 mL of ammonia solution. After vigorous stirring for 12 h at 25 °C, the resulting precipitates were collected *via* centrifugation, washed, and dried in an oven for 12 h. The dried sample was then annealed under a nitrogen atmosphere at 400 °C for 2 h, and followed by a temperature increased to 800 °C for 3 h. Finally, the HMCS were obtained by completely removing SiO<sub>2</sub> using 3 mol L<sup>-1</sup> NaOH at 60 °C.

### 2.2. Synthesis of N-(CuRu)<sub>NP+SA</sub>@NC hybrid, N-Ru<sub>NP+SA</sub>@NC, and (CuRu)<sub>NP+SA</sub>@NC

Hollow mesoporous carbon spheres (HMCS, 30 mg) acting as support were ultrasonically dispersed in deionized water (10 mL), followed by the addition of ruthenium acetylacetonate (40 mg) and copper acetylacetonate (20 mg), stirring, and ultrasonic treatment for 30 min. Next, an aqueous solution (6 mL) containing ascorbic acid (AA, 0.15 g) was incorporated, and the mixture was maintained at 60 °C for 9 h. The precursor was collected *via* centrifugation, washed three times and dried at 60 °C overnight. Subsequently, the CuRu@NC precursor underwent nitridation at 450 °C for 2 h, with a heating rate of 2 °C min<sup>-1</sup> in NH<sub>3</sub> atmosphere to produce the N-(CuRu)<sub>NP+SA</sub>@NC hybrid. For comparison, the preparation of N-Ru<sub>NP+SA</sub>@NC followed a similar procedure but without ruthenium acetylacetonate. (CuRu)<sub>NP+SA</sub>@NC was synthesized in the same manner as N-(CuRu)<sub>NP+SA</sub>@NC except that the pyrolysis atmosphere was changed to N<sub>2</sub>.

### 2.3. Materials characterization

Powder X-ray diffraction (XRD, Rigaku D/Max 2500V/PC, Japan, Cu K<sub>α</sub> radiation) was measured to characterize the crystal structure and phase composition. Scanning electron microscopy (SEM, FEI Quanta 200 FEG) and transmission electron microscopy (TEM, JEM-2100 F) were recorded to detect the morphology and elemental distribution. X-ray photoelectron spectroscopy (XPS, JPS-9010 Mg K<sub>α</sub>) was conducted to analyze the chemical state and electronic structure. Inductively coupled

plasma mass spectroscopy (ICP-MS, PerkinElmer corporation, Flexar-NexION300X) was applied to examine the metal contents of the catalysts. Raman spectra (Renishaw in Via) were obtained using a Renishaw in Via with a visible laser ( $k = 532$  nm).

#### 2.4. Electrochemical measurement

The electrocatalytic measurements were conducted in a typical three-electrode system through a CHI 760E (Shanghai, China) electrochemical workstation. Specifically, a glassy carbon electrode (GCE, diameter: 5.0 mm, disk area: 0.196 cm<sup>2</sup>) was selected as the working electrode, graphite rod and saturated KCl-filled with Ag/AgCl were applied as counter electrode and reference electrode, respectively. The potentials reported in this work were normalized versus the reversible hydrogen electrode (RHE) via a standard RHE calibration. The RHE calibration was conducted in high-purity H<sub>2</sub>-saturated with a Pt foil as the working electrode ( $E_{\text{Ag/AgCl}} + 0.197 + 0.059 \times \text{pH}$ ).

#### 2.5. Preparation of catalytic electrodes

To fabricate the working electrode, 3 mg of sample and 5  $\mu\text{L}$  of Nafion solution (5 wt%), were ultrasonically dispersed in deionized water-isopropanol solution (volume ratio, 1:1) to yield a homogeneous ink. Afterwards, 15  $\mu\text{L}$  well-dispersed ink was suspended onto the pre-polished glassy carbon electrode, and dried ink prior to measurement. The catalyst loading was

14.14  $\mu\text{g}_{\text{Ru}} \text{cm}^{-2}$ , which was calculated by ICP-MS data.

#### 2.6. Hydrogen oxidation reaction (HOR) measurements

Before HOR measurements, the electrolyte was bubbled with high purity H<sub>2</sub> for 30 min to maintain H<sub>2</sub>-saturated state during the HOR process. Cyclic voltammetry (CV) curves were first recorded between 0 and 1.0 V (vs. RHE) in N<sub>2</sub>-saturated 0.1 mol L<sup>-1</sup> KOH electrolyte until the stable curves were obtained. Then, the HOR polarization curves were gained at a sweep rate of 10 mV s<sup>-1</sup> from -0.05 to 0.50 V (vs. RHE) under 400, 900, 1600 and 2500 revolutions per minute (rpm) of the rotating disk electrode (RDE) rotation rate. The accelerated degradation tests were performed by cycling the samples ranging from 0 to 1.0 V (vs. RHE) with a scan rate of 100 mV s<sup>-1</sup> in H<sub>2</sub>-saturated 0.1 mol L<sup>-1</sup> KOH electrolyte. Chronoamperometric characterization was conducted at 50 mV (vs. RHE). LSV curve was recorded in H<sub>2</sub>-saturated (containing 1000 ppm CO) 0.1 mol L<sup>-1</sup> KOH electrolyte under 1600 rpm.

### 3. Results and discussion

#### 3.1. Synthesis and structure characterization

N-(CuRu)<sub>NP+SA</sub>@NC hybrids were fabricated using a simple impregnation and nitridation approach (Fig. 1(a)). This process commenced with the formation of monodisperse SiO<sub>2</sub>@DA solid spheres (DA: dopamine) (Fig. S1). Through calcination

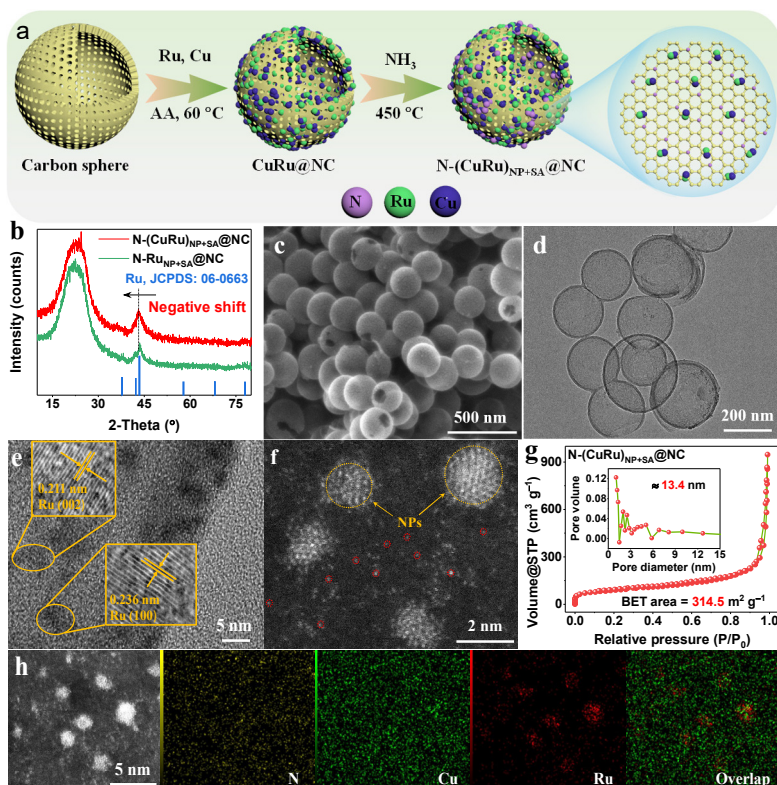


**Fig. 1.** Key characteristics of N-(CuRu)<sub>NP+SA</sub>@NC. (a) Schematic illustrations of the preparation of N-(CuRu)<sub>NP+SA</sub>@NC. (b) XRD patterns of N-(CuRu)<sub>NP+SA</sub>@NC and N-Ru<sub>NP+SA</sub>@NC. (c) SEM, (d) TEM and (e) high-resolution TEM images. (f) AC HAADF-STEM image of N-(CuRu)<sub>NP+SA</sub>@NC (The spots in the red dashed circle are attributed to Ru/Cu single atoms). (g) N<sub>2</sub> adsorption-desorption isotherms and pore size distribution (inset). (h) HAADF-STEM and corresponding elemental mappings images of N-(CuRu)<sub>NP+SA</sub>@NC.

and alkali-soaking, these solid spheres were transformed into hollow mesoporous carbon spheres (HMCS) with cracked surfaces and uniform size distributions (Fig. S2). Then, copper and ruthenium acetylacetonates were deposited onto the prepared HMCS using ascorbic acid (AA) as the reducing agent. The precursor was then nitrided in  $\text{NH}_3$  atmosphere to yield a dilute CuRu alloy and atomically dispersed Ru and Cu single-atom catalytic sites (Supporting Information). XRD patterns (Fig. 1(b)) of  $\text{N}-(\text{CuRu})_{\text{NP+SA}}@ \text{NC}$  show diffraction peaks consistent with metallic Ru in the hexagonal phase (JCPDS: 06-0663) [26]. The absence of a Cu peak suggests that the Cu concentration was extremely low, as confirmed by inductively coupled plasma mass spectroscopy (ICP-MS) data (Table S1). Compared to  $\text{N-Ru}_{\text{NP+SA}}@ \text{NC}$ , the  $\text{N}-(\text{CuRu})_{\text{NP+SA}}@ \text{NC}$  peak exhibited a slight shift to lower angle values, indicating the successful incorporation of a small amount of Cu into the Ru lattice and thus confirming the formation of dilute CuRu alloy nanoparticles [27].

As depicted in Fig. 1(c),  $\text{N}-(\text{CuRu})_{\text{NP+SA}}@ \text{NC}$  inherited the highly monodispersed hollow spherical morphology of HMCS. TEM observation verified the hollow and spherical nature of  $\text{N}-(\text{CuRu})_{\text{NP+SA}}@ \text{NC}$  (Fig. 1(d)). Hollow structures devoid of internal inert blocks offer advantages over solid spheres by shortening the transport distance of the reactants [25]. High-resolution TEM (HR-TEM) analysis of  $\text{N}-(\text{CuRu})_{\text{NP+SA}}@ \text{NC}$  revealed interplanar spacings of 0.211 and 0.236 nm, indexed to the (002) and (100) facets of metallic Ru, respectively (Fig. 1(e)). These spacings are lower than the standard Ru metal values (0.214 and 0.238 nm), further proving the alloying of Cu with Ru, which is consistent with the XRD findings. The aberration-corrected high-angle annular dark-field scanning transmission electron microscopy (HAADF-STEM) image of  $\text{N}-(\text{CuRu})_{\text{NP+SA}}@ \text{NC}$  in Fig. 1(f) reveals not only the presence of nanoparticles but also distinct single atoms. Fig. 1(g) and the inset showed that the Brunauer-Emmett-Teller (BET) surface area of  $\text{N}-(\text{CuRu})_{\text{NP+SA}}@ \text{NC}$  was  $314.5 \text{ m}^2 \text{ g}^{-1}$ , with the pore distribution indicating a mesoporous structure with an average pore size of 13.4 nm that results from the removal of the  $\text{SiO}_2$  core [28]. The large specific surface area and favorable mesoporous structure of  $\text{N}-(\text{CuRu})_{\text{NP+SA}}@ \text{NC}$  facilitated rapid electrolyte permeation and ion diffusion, accelerating the HOR kinetics [29]. As shown in Fig. 1(h), the distributions of Ru and Cu were further analyzed using HAADF-STEM and the corresponding elemental mapping images. In addition to coexisting on the alloy nanoparticles, Ru and Cu were observed as single atoms distributed on the HMCS.

### 3.2. Physicochemical characterization analysis

The valence states and local coordination of the metal atoms in  $\text{N}-(\text{CuRu})_{\text{NP+SA}}@ \text{NC}$  were characterized using X-ray absorption near-edge structure (XANES) and extended X-ray absorption fine structure (EXAFS) measurements [30]. The Ru K-edge XANES spectra (Fig. 2(a)) indicated that the absorption edge of  $\text{N}-(\text{CuRu})_{\text{NP+SA}}@ \text{NC}$  was positioned between those of the Ru foil and  $\text{RuO}_2$ , revealing that Ru predominantly existed in the  $\delta^+$  state ( $0 < \delta < 4$ ). A noticeable negative shift in the absorption energy of  $\text{N}-(\text{CuRu})_{\text{NP+SA}}@ \text{NC}$  compared to that of

$(\text{CuRu})_{\text{NP+SA}}@ \text{NC}$  suggests that N incorporation reduces the oxidation state of Ru [31,32]. The Ru K-edge Fourier transform (FT) EXAFS spectra and the fitting results (Fig. 2(b) and Fig. S3(a)) showed that the average distance for the first Ru-N/O shell in  $\text{N}-(\text{CuRu})_{\text{NP+SA}}@ \text{NC}$  was approximately 1.77 Å, which was significantly greater than those in  $(\text{CuRu})_{\text{NP+SA}}@ \text{NC}$  (1.68 Å) and  $\text{RuO}_2$  (1.48 Å). This finding strongly suggests that N incorporation not only reduces the oxidation state of Ru, but also leads to strong coordination between N and Ru [33]. Moreover,  $\text{N}-(\text{CuRu})_{\text{NP+SA}}@ \text{NC}$  displayed a clear second shell peak at 2.38 Å for Ru-Ru/Cu coordination, while the peak at 3.18 Å related to Ru-O-Ru scattering was absent, confirming the presence of isolated Ru atoms and CuRu alloy nanoparticles [34,35]. It is important to note that the Ru-Ru/Cu bond distance in  $\text{N}-(\text{CuRu})_{\text{NP+SA}}@ \text{NC}$  was slightly shorter than that of Ru foil (2.45 Å), suggesting the successful incorporation of Cu into the Ru lattice. The proximity of the Ru-Ru/Cu peak to that of Ru-Ru (Ru foil) reveals a low Cu content in the dilute RuCu alloy, which is consistent with the XRD results [23,36]. Additionally, the fitted coordination number for Ru-Ru/Cu in  $\text{N}-(\text{CuRu})_{\text{NP+SA}}@ \text{NC}$  was approximately 5, which is lower than the fitted coordination number of 12 for the Ru foil (Table S2), highlighting the existence of many coordination-unsaturated Ru sites on the catalyst surface, which can serve as the active phase during the HOR process [32]. The Ru atoms in both  $\text{N}-(\text{CuRu})_{\text{NP+SA}}@ \text{NC}$  and  $(\text{CuRu})_{\text{NP+SA}}@ \text{NC}$  exhibited similar coordination with comparable positions and intensities of the scattering peaks.

Similar trends were observed in the Cu K-edge XANES spectra (Fig. 2(c)), where the absorption energy of  $\text{N}-(\text{CuRu})_{\text{NP+SA}}@ \text{NC}$  was lower than that of CuO but higher than that of the Cu foil, approaching that of  $\text{Cu}_2\text{O}$ , and indicating that the average Cu valence state was close to +1. The EXAFS results (Fig. 2(d) and Fig. S3(b)) revealed Cu-N/O coordination at 1.52 Å and Cu-Ru coordination at 2.23 Å, demonstrating the coexistence of isolated Cu atoms and dilute CuRu nanoalloys within the  $\text{N}-(\text{CuRu})_{\text{NP+SA}}@ \text{NC}$  hybrid [30,37]. Notably,  $(\text{CuRu})_{\text{NP+SA}}@ \text{NC}$  did not show significant Cu-metal coordination, implying that Cu existed primarily in a monodisperse form, suggesting the effective reduction of dilute CuRu alloys by the nitriding process. The simultaneous presence of single Ru/Cu atoms and dilute CuRu alloy nanoparticles was further corroborated by the corresponding wavelet transform (WT) EXAFS analyses of the Ru and Cu K-edges (Figs. 2(e) and (f)). These results strongly validate the presence of atomically dispersed bimetallic Cu and Ru single atoms alongside dilute CuRu alloy in  $\text{N}-(\text{CuRu})_{\text{NP+SA}}@ \text{NC}$ .

Comprehensive XPS analysis provided detailed chemical and structural insights into  $\text{N}-(\text{CuRu})_{\text{NP+SA}}@ \text{NC}$ . The XPS survey spectrum confirms the presence of C, N, Cu, and Ru in  $\text{N}-(\text{CuRu})_{\text{NP+SA}}@ \text{NC}$  (Fig. S4). The C 1s peak was referenced to 284.0 eV as the calibration standard (Fig. S5). For the N 1s core-level spectra (Fig. S6), the peaks at 397.5, 398.4 and 400.0 eV were identified as pyridinic-N, N-M and pyrrolic-N, respectively [38,39]. The presence of the N-M bond in  $\text{N}-(\text{CuRu})_{\text{NP+SA}}@ \text{NC}$  was attributed to the successful coordination of nitrogen with the metal atoms (Cu and Ru) during nitri-

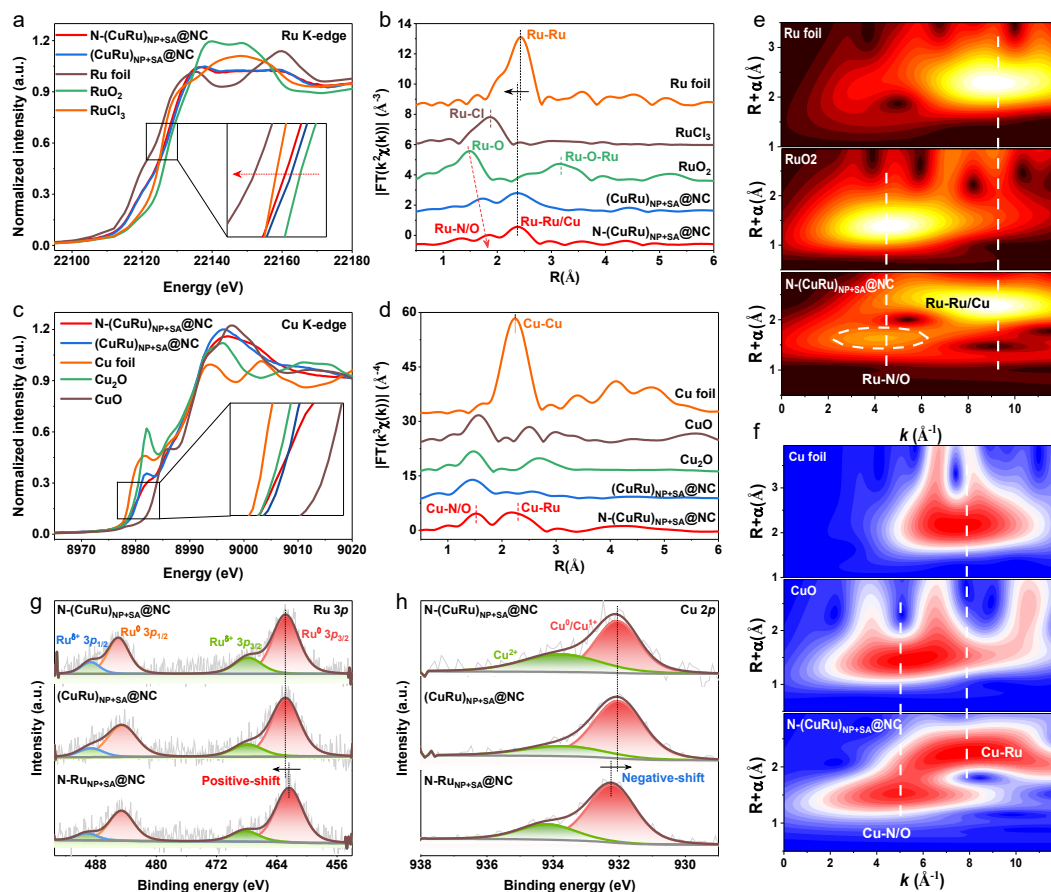


**Fig. 2.** Physicochemical characterization analysis. (a) Ru K-edge XANES spectra of N-(CuRu)<sub>NP+SA</sub>@NC, (CuRu)<sub>NP+SA</sub>@NC, Ru foil, RuCl<sub>3</sub> and RuO<sub>2</sub>. (b) Ru K-edge FT-EXAFS spectra. (c) Cu K-edge XANES of N-(CuRu)<sub>NP+SA</sub>@NC, (CuRu)<sub>NP+SA</sub>@NC, Cu foil, Cu<sub>2</sub>O and CuO. (d) Cu K-edge FT-EXAFS spectra. (e) Ru K-edge EXAFS WT analysis. (f) Cu K-edge EXAFS WT analysis. High-resolution XPS spectra of (g) Ru 3p, (h) Cu 2p in N-(CuRu)<sub>NP+SA</sub>@NC, (CuRu)<sub>NP+SA</sub>@NC, and N-Ru<sub>NP+SA</sub>@NC.

dation, facilitating strong interactions within the hybrid structure [40]. Fig. 2(g) shows two distinct peaks at 463.5 and 484.1 eV, corresponding to the Ru 3p<sub>3/2</sub> and Ru 3p<sub>1/2</sub> orbitals of metallic Ru. The peaks at 468.8 and 489.5 eV arose from the inevitable surface oxidation of the Ru species. Compared with N-Ru<sub>NP+SA</sub>@NC, N-(CuRu)<sub>NP+SA</sub>@NC showed a positive shift in the binding energy for Ru<sup>0</sup>, suggesting an electron-coupling effect between Ru and adjacent Cu in both the CuRu alloy and bimetallic single atoms [36]. The high-resolution Cu 2p XPS profiles (Fig. 2(h)) revealed deconvoluted peaks at 932.1 and 933.8 eV for Cu<sup>+</sup>/Cu and Cu<sup>2+</sup>, respectively. Strikingly, the Cu<sup>+</sup>/Cu peak in N-(CuRu)<sub>NP+SA</sub>@NC shifted to lower energies compared to that in N-Cu<sub>NP+SA</sub>@NC. The positive shift of the Ru peak and negative shift of the Cu peak verified the strong electronic interaction between Ru and Cu, that is, electron transfer from Ru to Cu. This electron transfer can lead to a decrease in the adsorption energy of Ru for H\* and CO\* and an increase in the adsorption energy of Cu for OH\*, which creates more favorable energetic conditions for the HOR reaction [41,42].

### 3.3. Electrochemical HOR performance

The HOR electrocatalytic performance of various catalysts was monitored using the RDE technique in H<sub>2</sub>-saturated 0.1

mol L<sup>-1</sup> KOH electrolyte. Calibration of the RHE was conducted prior to the electrochemical tests (Fig. S7). Initially, we examined the impact of nitriding temperature on the catalytic performance of N-(CuRu)<sub>NP+SA</sub>@NC, and the optimal temperature was found to be 450 °C (Fig. S8). Experimental investigation of the dependence of the reaction performance on the Ru content (Fig. S9) revealed an obvious volcano-shaped trend in the catalytic performance, with the highest activity achieved at the Ru loading of 3.08 wt%. This optimum Ru content likely arose from the synergistic interaction between the dilute CuRu-alloy nanoparticles and single Cu/Ru atoms with moderate concentration on the support, which maximized active site exposure and optimized intermediate adsorption [23]. The HOR activities of N-(CuRu)<sub>NP+SA</sub>@NC, (CuRu)<sub>NP+SA</sub>@NC, N-Ru<sub>NP+SA</sub>@NC, N-Cu<sub>NP+SA</sub>@NC, commercial Pt/C, and Ru/C were qualitatively compared based on their current responses (Fig. 3(a)). Notably, N-(CuRu)<sub>NP+SA</sub>@NC yielded the highest anode current density in both the kinetic- and diffusion-limited regions, indicating outstanding kinetic and intrinsic activity. By contrast, N-Cu<sub>NP+SA</sub>@NC exhibited poor HOR catalytic properties, suggesting that Ru acted as the primary active component for the HOR, with Cu modulating the Ru activity [43]. A comparison experiment in N<sub>2</sub>-saturated 0.1 mol L<sup>-1</sup> KOH electrolyte showed faint anodic current-voltage characteristics, confirming that the

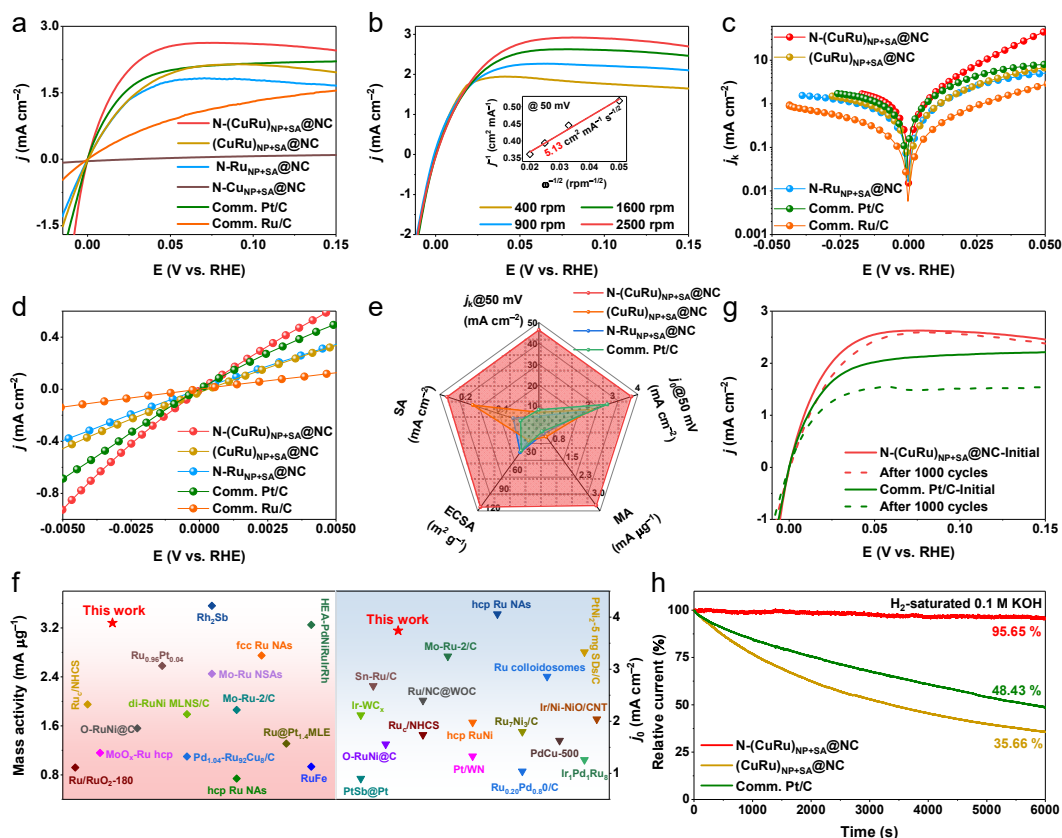


**Fig. 3.** Electrocatalytic HOR activity. (a) HOR polarization curves of different samples. (b) HOR polarization curves of N-(CuRu)<sub>NP+SA</sub>@NC at different rotation speeds. Inset shows corresponding Koutecky-Levich plot. (c) Tafel plots. (d) Linear fitting curves in micro-polarization region. (e) Comparison of various performance parameters of the obtained MA and  $j_0$  with those of recently reported alkaline HOR electrocatalysts. (f) Comparison of HOR electrocatalysts. (g) HOR polarization curves for N-(CuRu)<sub>NP+SA</sub>@NC and comm. Pt/C before and after 1000 cycles. (h) Relative current-time chronoamperometry responses of different catalysts in pure H<sub>2</sub>-saturated 0.1 mol L<sup>-1</sup> KOH.

anode current predominantly resulted from H<sub>2</sub> oxidation (Fig. S10). Furthermore, the polarization curves at varying rotating speeds (Fig. 3(b)) demonstrate that the limiting current density increased with the rotational rate, confirming that the reaction was controlled by H<sub>2</sub> mass transfer [44]. Using the Koutecky-Levich equation, a calibrated slope of 5.13 cm<sup>2</sup> mA<sup>-1</sup> s<sup>-1/2</sup> was obtained at 50 mV vs. RHE for N-(CuRu)<sub>NP+SA</sub>@NC (inset in Fig. 3(b)), in agreement with the theoretical value (4.87 cm<sup>2</sup> mA<sup>-1</sup> s<sup>-1/2</sup>) for the two-electron HOR system [45]. To thoroughly probe the HOR catalytic mechanism, the Tafel slopes were determined by plotting the kinetic current density ( $j_k$ ) against the overpotential of the as-prepared samples (Fig. 3(c)). The asymmetrical behavior of the Tafel plot suggested that N-(CuRu)<sub>NP+SA</sub>@NC followed the Heyrovsky-Volmer mechanism, with the Volmer step as the rate-determining step (RDS) [46].

As plotted in Fig. 3(d), the exchange current density ( $j_0$ ) of N-(CuRu)<sub>NP+SA</sub>@NC was evaluated as 3.74 mA cm<sup>-2</sup> by fitting the micro-polarization region, exceeding those of the (CuRu)<sub>NP+SA</sub>@NC (2.12 mA cm<sup>-2</sup>), N-Ru<sub>NP+SA</sub>@NC (1.95 mA cm<sup>-2</sup>) and Pt/C (2.77 mA cm<sup>-2</sup>) catalysts, and implying superior inherent HOR activity of N-(CuRu)<sub>NP+SA</sub>@NC (Fig. 3(e)). Moreover, N-(CuRu)<sub>NP+SA</sub>@NC captured a geometric  $j_k$  of 7.94 mA cm<sup>-2</sup> at 25 mV. At 50 mV, N-(CuRu)<sub>NP+SA</sub>@NC showed the highest  $j_k$  value of 46.34 mA cm<sup>-2</sup>, with 6.7-fold, 9.1-fold and 5.7-fold in-

creases compared to those of (CuRu)<sub>NP+SA</sub>@NC (6.89 mA cm<sup>-2</sup>), N-Ru<sub>NP+SA</sub>@NC (5.07 mA cm<sup>-2</sup>), and Pt/C (8.12 mA cm<sup>-2</sup>), respectively. The mass activity (MA) at 50 mV was derived by normalizing the  $j_k$  value to the mass determined by ICP-MS, allowing for a more accurate reflection of the HOR activity. N-(CuRu)<sub>NP+SA</sub>@NC demonstrated an MA of 3.28 mA μg<sub>Ru</sub><sup>-1</sup>, remarkably higher than those of (CuRu)<sub>NP+SA</sub>@NC (0.42 mA μg<sub>Ru</sub><sup>-1</sup>), N-Ru<sub>NP+SA</sub>@NC (0.29 mA μg<sub>Ru</sub><sup>-1</sup>) and commercial Pt/C (0.20 mA μg<sub>Ru</sub><sup>-1</sup>). Considering that Ru can affect the hydrogen adsorption/desorption potential region (H<sub>upd</sub>), CO stripping voltammetry was adopted to evaluate the electrochemical surface area (ECSA) and identify the electrocatalytically active sites (Table S4) [47]. The ECSA for N-(CuRu)<sub>NP+SA</sub>@NC was calculated as 128.93 m<sup>2</sup> g<sup>-1</sup>, higher than those of the compared samples (Fig. 3(e)). Additionally, N-(CuRu)<sub>NP+SA</sub>@NC exhibited the highest specific activity among all of the catalysts. In short, N-(CuRu)<sub>NP+SA</sub>@NC showed exemplary electrocatalytic performance, as evidenced by its superiority in various performance parameters (Table S4). Compared to other previously reported catalysts (Fig. 3(f) and Table S5), N-(CuRu)<sub>NP+SA</sub>@NC also showed a noteworthy superiority in  $j_0$  and MA.

Long-term stability is a vital criterion for assessing the suitability of HOR electrocatalysts for practical applications. As shown in Fig. 3(g), little degradation in the HOR activity was

observed for N-(CuRu)<sub>NP+SA</sub>@NC after 1000 cycles, whereas a drastic decay in the activity was observed for commercial Pt/C. The stability of N-(CuRu)<sub>NP+SA</sub>@NC was evaluated by chronoamperometry at 50 mV. As shown in Fig. 3(h), a decay of only 4.35% was observed for N-(CuRu)<sub>NP+SA</sub>@NC after 6000 s of continuous operation. In sharp contrast, under the same conditions, the HOR activities of Pt/C and (CuRu)<sub>NP+SA</sub>@NC decreased by 51.57% and 64.34%, respectively. The morphology of N-(CuRu)<sub>NP+SA</sub>@NC after stabilization was retained well, as verified by SEM (Fig. S11). These results strongly demonstrate the durability of N-(CuRu)<sub>NP+SA</sub>@NC in the alkaline HOR process.

Generally, hydrogen and hydroxyl adsorption on an electrocatalyst surface plays a key role in HOR activity under alkaline conditions [48,49]. To ascertain the catalytic mechanism underlying the remarkable HOR performance of the N-(CuRu)<sub>NP+SA</sub>@NC hybrid, we investigated the adsorption capacity of H and OH species using the CV and CO-stripping techniques, respectively. The desorption of hydrogen under-potential deposition ( $H_{\text{upd}}$ ) on the CV curve is a promising approach for estimating the strength of  $H_{\text{ad}}$  bonds. As shown in Fig. 4(a), the  $H_{\text{upd}}$  peak potential of N-(CuRu)<sub>NP+SA</sub>@NC was 0.157 V, which is more negative than those of N-Ru<sub>NP+SA</sub>@NC (0.182 V), (CuRu)<sub>NP+SA</sub>@NC (0.185 V), and Pt/C (0.323 V), indicating a weaker HBE. The attenuated HBE originates from the synergistic effect of the Cu and Ru species and the N coordination effect, resulting in a lower Ru–H bond energy. Analogously, CO-stripping measurements were conducted to explore the OH adsorption strength, as the adsorbed OH\* can expedite the oxidation of the CO\* adsorbed intermediate to CO<sub>2</sub> ( $\text{OH}^* + \text{CO}^* \rightarrow \text{CO}_2 + \text{H}^+ + \text{e}^-$ ) [40,50]. As shown in Fig. 4(b), N-(CuRu)<sub>NP+SA</sub>@NC showed a CO-stripping peak at 0.715 V,

which is shifted negatively compared to those of N-Ru<sub>NP+SA</sub>@NC (0.736 V), (CuRu)<sub>NP+SA</sub>@NC (0.730 V), and Pt/C (0.741 V). This confirmed that N-(CuRu)<sub>NP+SA</sub>@NC exhibits stronger binding with OH\* that endows it with more unpoisoned active sites to enhance HOR performance. Additionally, zeta potential measurements further confirmed the strongest hydroxyl adsorption on N-(CuRu)<sub>NP+SA</sub>@NC (Fig. 4(c) and Fig. S12). As anticipated, the anodic HOR current of N-(CuRu)<sub>NP+SA</sub>@NC declined slightly in the H<sub>2</sub>-saturated electrolyte containing 1000 ppm CO (Fig. 4(d)), confirming that strong OH\* adsorption can efficiently oxidize CO to prevent catalyst poisoning, resulting in excellent CO tolerance [51]. In stark contrast, the current density of Pt/C decreased sharply relative to the initial state (Fig. 4(e)), indicating that the active sites on its catalytic surface were almost completely occupied or poisoned by CO, blocking the hydrogen adsorption/dissociation sites [52]. To further examine the temporal evolution of the CO tolerance of the samples, we conducted tests at a continuous overpotential of 50 mV to obtain the chronoamperometric response curves (Fig. 4(f)). After a stability test for 1200 s, the relative current density of N-(CuRu)<sub>NP+SA</sub>@NC was maintained at 93.12%, significantly surpassing that of commercial Pt/C (27.11%). This comprehensive analysis underscores the enhanced HOR activity and CO tolerance of N-(CuRu)<sub>NP+SA</sub>@NC, which can be attributed to its optimal hydrogen and hydroxyl adsorption properties.

### 3.4. Theoretical study

To gain insight into the enhanced catalytic performance of N-(CuRu)<sub>NP+SA</sub>@NC, density functional theory (DFT) calculations were performed using three theoretical models (Fig. S13). The (001) lattice plane of Ru was selected for the simulations

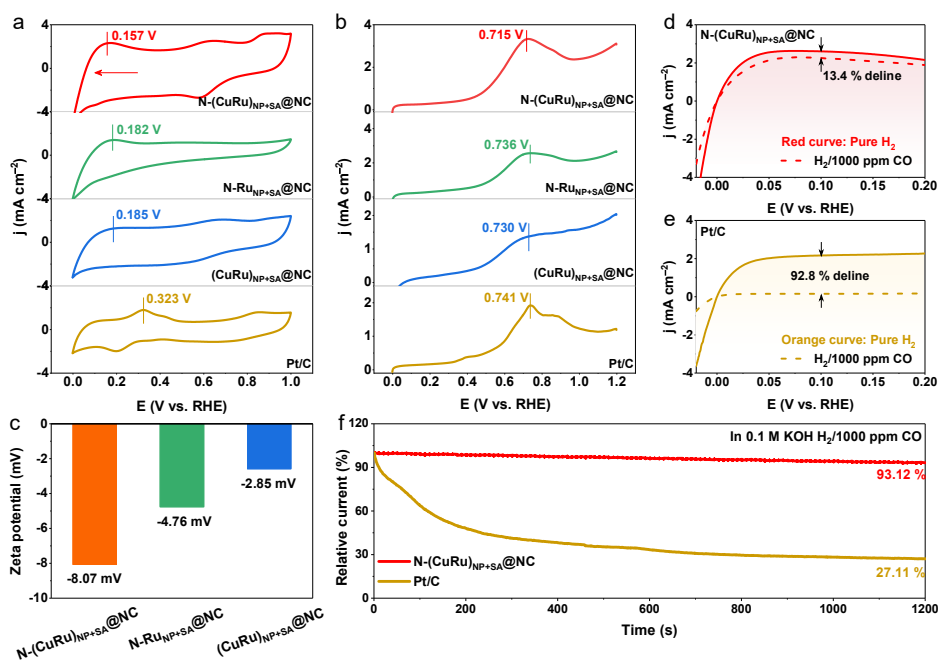


**Fig. 4.** CV curves (a) and CO-stripping voltammograms (b) of N-(CuRu)<sub>NP+SA</sub>@NC, (CuRu)<sub>NP+SA</sub>@NC, N-Ru<sub>NP+SA</sub>@NC and Pt/C. (c) Zeta potential of N-(CuRu)<sub>NP+SA</sub>@NC, (CuRu)<sub>NP+SA</sub>@NC, N-Ru<sub>NP+SA</sub>@NC. HOR polarization curves of N-(CuRu)<sub>NP+SA</sub>@NC (d) and Pt/C (e) in 1000 ppm CO/H<sub>2</sub>-saturated 0.1 mol L<sup>-1</sup> KOH. (f) Chronoamperometry ( $j-t$ ) response at 50 mV in H<sub>2</sub>/1000 ppm CO-saturated 0.1 mol L<sup>-1</sup> KOH.

based on its structural properties and crystal facet stability. The differential charge density distributions (Fig. 5(a)) reveal significant charge accumulation at the Cu-Ru interface, indicating a strong interaction that leads to charge redistribution, which is consistent with the XPS findings. The total density of states (DOS) of the N-(CuRu)<sub>NP+SA</sub>@NC electrocatalysts displayed a higher occupation at the Fermi level compared to (CuRu)<sub>NP+SA</sub>@NC and N-Ru<sub>NP+SA</sub>@NC, suggesting that the electronic coupling between Ru and Cu diminished the charge transfer resistance (Fig. 5(b)) [43]. This also indicates that more electronic states are accessible for electron occupation and movement at this specific energy level, thereby enhancing electronic conductivity. The *d*-band center of N-(CuRu)<sub>NP+SA</sub>@NC is slightly elevated relative to those of (CuRu)<sub>NP+SA</sub>@NC and N-Ru<sub>NP+SA</sub>@NC, as observed from the partial density of states (pDOS) diagram (Fig. 5(c)). According to the *d*-band center theory, this upward shift indicates enhanced adsorption strength for reaction intermediates on Ru sites, promoting H<sub>2</sub>O formation. These results imply that the metal-metal interactions can induce charge redistribution and modify the energy band structure [53].

HBE and OHBE are essential descriptors for assessing the HOR performance [54]. Following the Sabatier principle, achieving an HBE value close to zero is crucial for balancing hydrogen adsorption and desorption, thereby optimizing HOR efficiency [55]. Simultaneously, higher OHBE, in line with bifunctional theory, supports effective OH adsorption, which is vital for the Volmer process that generates water [56]. Simulations of H\* and OH\* adsorption on the N-(CuRu)<sub>NP+SA</sub>@NC, (CuRu)<sub>NP+SA</sub>@NC, and N-Ru<sub>NP+SA</sub>@NC samples were performed.

As shown in Fig. 5(d), N-(CuRu)<sub>NP+SA</sub>@NC exhibited a favorable HBE value of  $-0.19$  eV for H\* adsorption. Moreover, the OHBE values for (CuRu)<sub>NP+SA</sub>@NC and N-Ru<sub>NP+SA</sub>@NC were 0.14 and 0.26 eV, respectively, indicating weak OH adsorption that impeded HOR catalysis (Fig. 5(d)). Conversely, N-(CuRu)<sub>NP+SA</sub>@NC demonstrated a stronger OH adsorption capability with an OHBE of  $-0.09$  eV, suggesting nearly optimal HBE and OHBE values that significantly enhance HOR kinetics. Compared to (CuRu)<sub>NP+SA</sub>@NC and N-Ru<sub>NP+SA</sub>@NC, the CO adsorption energy on the surface of the N-(CuRu)<sub>NP+SA</sub>@NC catalyst was the weakest, indicating that the modulation by Cu and N doping significantly regulated the electronic structure of Ru, thereby enhancing CO poisoning resistance (Fig. 5(e)).

Free energy diagrams of the alkaline HOR pathways over N-(CuRu)<sub>NP+SA</sub>@NC, (CuRu)<sub>NP+SA</sub>@NC, and N-Ru<sub>NP+SA</sub>@NC are presented in Fig. 5(f). The initial steps involve exergonic H adsorption, while the Volmer step can be divided into OH adsorption and the subsequent recombination of OH\* and H\* to form water [57]. Notably, the H\* + OH\* steps were endothermic, with energy barriers of 0.39, 0.61 and 0.86 eV for N-(CuRu)<sub>NP+SA</sub>@NC, (CuRu)<sub>NP+SA</sub>@NC and N-Ru<sub>NP+SA</sub>@NC, respectively, while water formation steps were exergonic. Analysis of these energy values revealed that the potential-determining step (PDS) of all the catalysts was the H\* + OH\* step, with N-(CuRu)<sub>NP+SA</sub>@NC demonstrating the lowest energy barrier. The low energy barrier of N-(CuRu)<sub>NP+SA</sub>@NC was primarily due to the synergistic effect between the alloy nanoparticles and single atoms, along with the incorporation of N, which collectively altered the adsorption configuration and electronic state of the reaction intermediates, thereby enhanc-

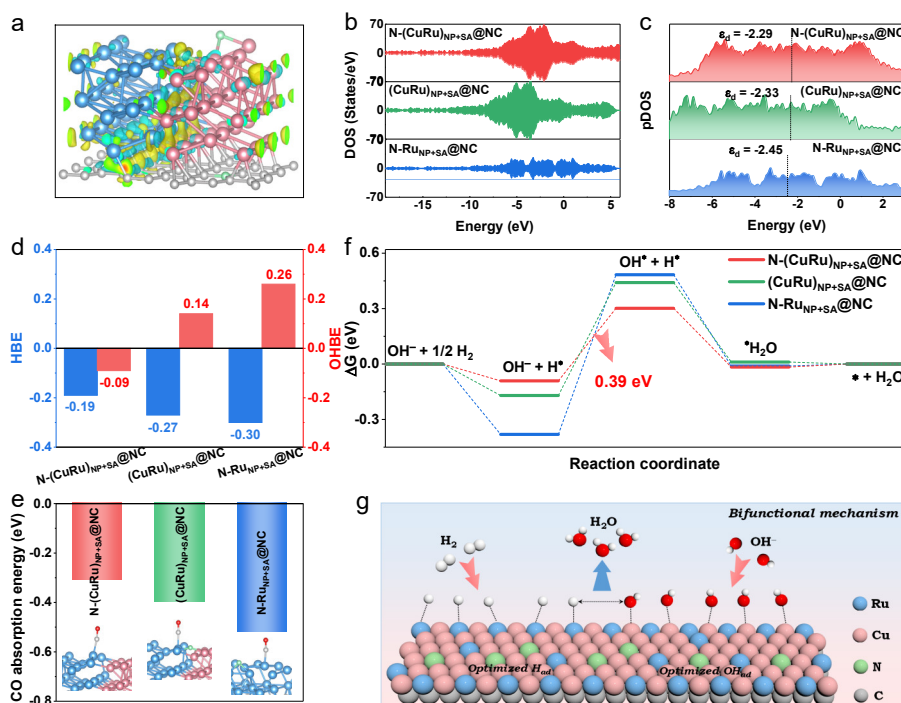


**Fig. 5.** (a) Differential charge density distributions of N-(CuRu)<sub>NP+SA</sub>@NC. The blue, green and pink spheres represented Ru, N and Cu atoms, respectively. (b) Density of state (DOS) plots. (c) The pDOS diagram for the *d* orbitals of metals in N-(CuRu)<sub>NP+SA</sub>@NC, (CuRu)<sub>NP+SA</sub>@NC, N-Ru<sub>NP+SA</sub>@NC. (d) Calculated HBE and OHBE values. (e) CO adsorption energies on N-(CuRu)<sub>NP+SA</sub>@NC, (CuRu)<sub>NP+SA</sub>@NC and N-Ru<sub>NP+SA</sub>@NC models. (f) Calculated energy profile for hydrogen oxidation into H<sub>2</sub>O. (g) Schematic illustration of HOR catalysis on N-(CuRu)<sub>NP+SA</sub>@NC.

ing HOR activity and CO tolerance. Fig. 5(g) visually depicts the HOR catalytic mechanism in the N-(CuRu)<sub>NP+SA</sub>@NC model to better understand the reaction process.

#### 4. Conclusions

In summary, we developed a N-(CuRu)<sub>NP+SA</sub>@NC electrocatalyst using an effective ammonia N-(CuRu)<sub>NP+SA</sub>@NC assisted gas N-(CuRu)<sub>NP+SA</sub>@NC phase nitridation strategy. This electrocatalyst features dilute CuRu alloy nanoparticles and mono-dispersed Cu and Ru dual single atoms confined on N-doped hollow mesoporous microspheres. Its unique microstructure and interconnected mesoporosity maximize atomic utilization and exposed active catalytic sites. The resulting N-(CuRu)<sub>NP+SA</sub>@NC showed excellent HOR activity, stability, and CO poisoning resistance that are superior to those of (CuRu)<sub>NP+SA</sub>@NC, N-Ru<sub>NP+SA</sub>@NC, and most contemporary noble-metal-based catalysts. Experimental and DFT results revealed that dilute alloying and single-atom dispersion of the introduced Cu regulated the electronic structure of the host Ru, reducing H\* and CO\* adsorption while enhancing OH\* adsorption on the N-(CuRu)<sub>NP+SA</sub>@NC electrocatalyst, which significantly improved the catalytic performance and CO resistance. These findings underscore the importance of rationally designing high-activity alkaline HOR catalysts by appropriately tuning the adsorption of intermediates on the catalyst surface, which is of great significance for the commercial development of AEMFCs.

#### Declaration of competing interest

The authors declare that they have no known competing financial interests or personal relationships that could have appeared to influence the work reported in this paper.

#### Electronic supporting information

Supporting information is available in the online version of this article.

#### References

- [1] J. Cai, X. Zhang, Z. Lyu, H. Huang, S. Wang, L. Fu, Q. Wang, X.-F. Yu, Z. Xie, S. Xie, *ACS Catal.*, **2023**, 13, 6974–6982.
- [2] C. Huang, M. Feng, Y. Peng, B. Zhang, J. Huang, X. Yue, S. Huang, *Adv. Funct. Mater.*, **2023**, 33, 2300593.
- [3] P. Han, N. Yao, W. Zuo, W. Luo, *Chin. J. Catal.*, **2022**, 43, 1527–1534.
- [4] Y. Men, D. Wu, Y. Hu, L. Li, P. Li, S. Jia, J. Wang, G. Cheng, S. Chen, W. Luo, *Angew. Chem. Int. Ed.*, **2023**, 62, e202217976.
- [5] L. Du, H. Xiong, H. Lu, L.-M. Yang, R.-Z. Liao, B.Y. Xia, B. You, *Exploration*, **2022**, 2, 20220024.
- [6] Z. Yao, T. Tang, Z. Jiang, L. Wang, J. Hu, L. Wan, *ACS Nano*, **2022**, 16, 5153–5183.
- [7] Z. Zhang, H. Liu, L. Ni, Z. Zhao, H. Li, *J. Energy Chem.*, **2022**, 72, 176–185.
- [8] X. Zhang, L. Xia, G. Zhao, B. Zhang, Y. Chen, J. Chen, M. Gao, Y. Jiang, Y. Liu, H. Pan, W. Sun, *Adv. Mater.*, **2023**, 35, 2208821.
- [9] D. Strmcnik, M. Uchimura, C. Wang, R. Subbaraman, N. Danilovic, D. van der Vliet, A.P. Paulikas, V.R. Stamenkovic, N.M. Markovic, *Nat. Chem.*, **2013**, 5, 300–306.
- [10] P. Han, X. Yang, L. Wu, H. Jia, J. Chen, W. Shi, G. Cheng, W. Luo, *Adv. Mater.*, **2023**, 36, 2304496.
- [11] Y. Zhou, Z. Xie, J. Jiang, J. Wang, X. Song, Q. He, W. Ding, Z. Wei, *Nat. Catal.*, **2020**, 3, 454–462.
- [12] C. Yang, j. Yue, G. Wang, W. Luo, *Angew. Chem. Int. Ed.*, **2024**, 63, e202401453.
- [13] J. Mao, C. T. He, J. Pei, Y. Liu, J. Li, W. Chen, D. He, D. Wang, Y. Li, *Nano Lett.*, **2020**, 20, 3442–3448.
- [14] P. O. L. Han, W. Liu, X. Wang, H.-T. Wang, R. Zhang, C.-W. Pao, X. Liu, W.-F. Pong, J. Song, Z. Zhuang, M. V. Mirkin, J. Luo, H. L. Xin, *Sci. Adv.*, **2022**, 8, 2664.

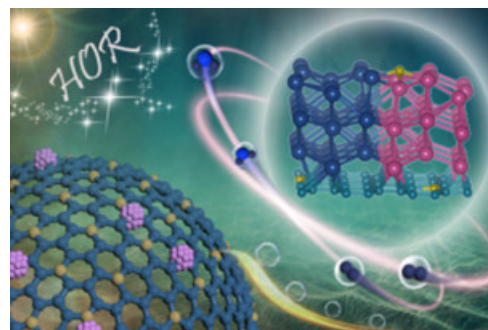
#### Graphical Abstract

*Chin. J. Catal.*, 2025, 72: 266–276 doi: 10.1016/S1872-2067(25)64670-5

#### Boosting the Volmer step by synergistic coupling of dilute CuRu nanoalloy with Cu/Ru dual single atoms for efficient and CO-tolerant alkaline hydrogen oxidation

Yi Liu, Shuqing Zhou, Chenggong Niu, Tayirjan Taylor Isimjan, Yongfa Zhu, Dingsheng Wang, Xiulin Yang\*, Jieshan Qiu\*, Bin Wu\*  
*Guangxi Normal University, China;*  
*King Abdullah University of Science and Technology (KAUST), Saudi Arabia;*  
*Tsinghua University, China;*  
*Beijing University of Chemical Technology, China;*  
*Nanyang Technological University, Singapore*

A unique N-(CuRu)<sub>NP+SA</sub>@NC electrocatalyst consisting of dilute CuRu alloy nanoparticles and dual Cu/Ru single atoms can achieve efficient HOR activity and stability, as well as strong anti-CO resistance ability. Experiment result reveals that the dilute alloying and monoatomization of foreign Cu tailor the electron structure of host Ru, resulting in reduced adsorption of H\* and CO\* and an enhanced adsorption of OH\*, thereby significantly enhancing the HOR activity and CO resistance.



- [15] X. Mu, S. Liu, M. Zhang, Z. Zhuang, D. Chen, Y. Liao, H. Zhao, S. Mu, D. Wang, Z. Dai, *Angew. Chem. Int. Ed.*, **2024**, 63, e202319618.
- [16] L. Wang, J. Wu, S. Wang, H. Liu, Y. Wang, D. Wang, *Nano Res.*, **2024**, 17, 3261–3301.
- [17] L. Qi, X. Bai, Y. Wang, Z. Duan, L. Li, J. Guan, *CCS Chem.*, **2025**, <https://doi.org/10.31635/ccschem.31024.202404810>.
- [18] X. Bai, J. Han, S. Chen, X. Niu, J. Guan, *Chin. J. Catal.*, **2023**, 54, 212–219.
- [19] X. Xu, J. Guan, *Mater. Sci. Eng. R Rep.*, **2025**, 162, 100886.
- [20] T. Tang, Y. Wang, J. Han, Q. Zhang, X. Bai, X. Niu, Z. Wang, J. Guan, *Chin. J. Catal.*, **2023**, 46, 48–55.
- [21] C. Hu, E. Song, M. Wang, W. Chen, F. Huang, Z. Feng, J. Liu, J. Wang, *Adv. Sci.*, **2021**, 8, 2001881.
- [22] Z. Dong, Y. Nan, T. Tang, X.-Z. Liu, J. Fu, H.-R. Pan, Z. Jiang, L. Ding, X. Cheng, L.-R. Zheng, J. Zhang, X. Chang, B. Xu, J.-S. Hu, *ACS Catal.*, **2023**, 13, 7822–7830.
- [23] Z. Cui, Z. Ren, C. Ma, B. Chen, G. Chen, R. Lu, W. Zhu, T. Gan, Z. Wang, Z. Zhuang, Y. Han, *Angew. Chem. Int. Ed.*, **2024**, 63, e202404761.
- [24] Y. Zhao, X. Wang, Z. Li, P. Zhao, C. Tao, G. Cheng, W. Luo, *Chin. Chem. Lett.*, **2022**, 33, 1065–1069.
- [25] S. Gong, W. Wang, C. Zhang, M. Zhu, R. Lu, J. Ye, H. Yang, C. Wu, J. Liu, D. Rao, S. Shao, X. Lv, *Adv. Funct. Mater.*, **2022**, 32, 2110649.
- [26] Y. Guo, W. He, X. Tan, Y. Xiao, B. Du, C. Wang, H. Cui, Y. Li, C. Wang, *Adv. Funct. Mater.*, **2024**, 34, 2412142.
- [27] X. Zhang, Z. Li, X. Sun, L. Wei, H. Niu, S. Chen, Q. Chen, C. Wang, F. Zheng, *ACS Mater. Lett.*, **2022**, 4, 2097–2105.
- [28] M. Guo, Z. Huang, Y. Qu, L. Wang, H. Li, T.T. Isimjan, X. Yang, *Appl. Catal. B Environ.*, **2023**, 320, 121991.
- [29] S. Liang, L. Zou, L. Zheng, F. Li, X. Wang, L. Song, J. Xu, *Adv. Energy Mater.*, **2022**, 12, 2103097.
- [30] Y. Cai, J. Fu, Y. Zhou, Y.-C. Chang, Q. Min, J.-J. Zhu, Y. Lin, W. Zhu, *Nat. Commun.*, **2021**, 12, 586.
- [31] J. Hu, B. Xu, J. Xu, S. Li, Z. Liu, C. Lu, Y. Feng, K. Feng, J. Zhong, *J. Energy Chem.*, **2023**, 87, 24–31.
- [32] H. Zhang, H. Su, M.A. Soldatov, Y. Li, X. Zhao, M. Liu, W. Zhou, X. Zhang, X. Sun, Y. Xu, P. Yao, S. Wei, Q. Liu, *Small*, **2021**, 17, 2105231.
- [33] H. Jia, N. Yao, Y. Jin, L. Wu, J. Zhu, W. Luo, *Nat. Commun.*, **2024**, 15, 5419.
- [34] T. Zheng, C. Liu, C. Guo, M. Zhang, X. Li, Q. Jiang, W. Xue, H. Li, A. Li, C.-W. Pao, J. Xiao, C. Xia, J. Zeng, *Nat. Nanotechnol.*, **2021**, 16, 1386–1393.
- [35] J. Zhuang, D. Wang, *Mater. Today Catal.*, **2023**, 2, 100009.
- [36] J. Lan, Z. Wei, Y.R. Lu, D. Chen, S. Zhao, T.S. Chan, Y. Tan, *Nat. Commun.*, **2023**, 14, 2870.
- [37] F. Ma, P. Zhang, X. Zheng, L. Chen, Y. Li, Z. Zhuang, Y. Fan, P. Jiang, H. Zhao, J. Zhang, Y. Dong, Y. Zhu, D. Wang, Y. Wang, *Angew. Chem. Int. Ed.*, **2024**, 63, e202412785.
- [38] Z. Luo, Q. Peng, Z. Huang, L. Wang, Y. Yang, J. Dong, T.T. Isimjan, X. Yang, *J. Colloid Interface Sci.*, **2023**, 629, 111–120.
- [39] Z. Liu, D. Liu, L. Zhao, J. Tian, J. Yang, L. Feng, *J. Mater. Chem. A*, **2021**, 9, 7750–7758.
- [40] X. Wang, H. Yao, C. Zhang, C. Li, K. Tong, M. Gu, Z. Cao, M. Huang, H. Jiang, *Adv. Funct. Mater.*, **2023**, 33, 2301804.
- [41] Q. Wu, M. Luo, J. Han, W. Peng, Y. Zhao, D. Chen, M. Peng, J. Liu, F. M. F. de Groot, Y. Tan, *ACS Energy Lett.*, **2020**, 5, 192–199.
- [42] Y. Dong, Z. Zhang, W. Yan, X. Hu, C. Zhan, Y. Xu, X. Huang, *Angew. Chem. Int. Ed.*, **2023**, 62, e202311722.
- [43] L. Wang, Z. Xu, C. Kuo, J. Peng, F. Hu, L. Li, H. Chen, J. Wang, S. Peng, *Angew. Chem. Int. Ed.*, **2023**, 62, e202311937.
- [44] G. Meng, H. Cao, T. Wei, Q. Liu, J. Fu, S. Zhang, J. Luo, X. Liu, *Chem. Commun.*, **2022**, 58, 11839–11842.
- [45] L. An, S. Deng, X. Guo, X. Liu, T. Zhao, K. Chen, Y. Zhu, Y. Fu, X. Zhao, D. Wang, *Chin. J. Catal.*, **2022**, 43, 3154–3160.
- [46] X. Tian, P. Zhao, W. Sheng, *Adv. Mater.*, **2019**, 31, 1808066.
- [47] B. Qin, H. Yu, X. Gao, D. Yao, X. Sun, W. Song, B. Yi, Z. Shao, *J. Mater. Chem. A*, **2018**, 6, 20374–20382.
- [48] L. Wang, S. Meng, C. Tang, C. Zhan, S. Geng, K. Jiang, X. Huang, L. Bu, *ACS Nano*, **2023**, 17, 17779–17789.
- [49] C. Yang, Y. Li, C. Ge, W. Jiang, G. Cheng, L. Zhuang, W. Luo, *Chin. J. Chem.*, **2022**, 40, 2495–2501.
- [50] S. Qin, Y. Duan, X. Zhang, L.-R. Zheng, F.-Y. Gao, P.-P. Yang, Z.-Z. Niu, R. Liu, Y. Yang, X.-S. Zheng, J.-F. Zhu, M.-R. Gao, *Nat. Commun.*, **2021**, 12, 2686.
- [51] X. Zhang, S. Hu, Y. Wang, L. Shi, Y. Yang, M.-R. Gao, *Nano Lett.*, **2023**, 23, 107–115.
- [52] G. Yang, Y. Yang, H. Qu, Y. Wang, C. Ru, H. Wu, Y. Han, J. Zhu, M. Xiao, C. Liu, W. Xing, *Mater. Today Phys.*, **2024**, 40, 101312.
- [53] X. Song, X. Zhang, Y. Deng, Z. Nan, W. Song, Y. Wang, L. Lü, Q. Jiang, X. Jin, Y. Zheng, M. Chen, Z. Xie, J.-F. Li, Z.-Q. Tian, F.R. Fan, *J. Am. Chem. Soc.*, **2023**, 145, 12717–12725.
- [54] X. Yang, B. Ouyang, P. Shen, Y. Sun, Y. Yang, Y. Gao, E. Kan, C. Li, K. Xu, Y. Xie, *J. Am. Chem. Soc.*, **2022**, 144, 11138–11147.
- [55] L. Li, S. Liu, C. Zhan, Y. Wen, Z. Sun, J. Han, T. Chan, Q. Zhang, Z. Hu, X. Huang, *Energy Environ. Sci.*, **2023**, 16, 157–166.
- [56] Z. Tian, X. Han, J. Du, Z. Li, Y. Ma, Z. Han, *ACS Appl. Mater. Interfaces*, **2023**, 15, 11853–11865.
- [57] L. Su, Y. Zhao, Y. Jin, X. Fan, Z. Liu, W. Luo, *J. Mater. Chem. A*, **2022**, 10, 21856–21861.

## 稀CuRu合金与Cu/Ru双单原子的协同耦合加速碱性氢氧化的Volmer动力学

刘奕<sup>a</sup>, 周树清<sup>a</sup>, 牛成功<sup>a</sup>, 塔伊尔詹·泰勒·伊西姆詹<sup>b</sup>, 朱永法<sup>c</sup>, 王定胜<sup>c</sup>, 杨秀林<sup>a,\*</sup>,  
邱介山<sup>d,\*</sup>, 武斌<sup>e,\*</sup>

<sup>a</sup>广西师范大学化学与药学院, 广西低碳能源材料重点实验室, 广西桂林541004, 中国

<sup>b</sup>阿卜杜拉国王科技大学的沙特阿拉伯基础工业公司, 图瓦23955-6900, 沙特阿拉伯

<sup>c</sup>清华大学化学系, 北京100084, 中国

<sup>d</sup>北京化工大学化工学院, 化工资源工程国家重点实验室, 北京100029, 中国

<sup>e</sup>新加坡南洋理工大学材料科学与工程学院, 新加坡639798, 新加坡

**摘要:** 碱性阴离子交换膜燃料电池(AEMFCs)因阴极可采用非贵金属催化氧化还原而备受关注。然而, 阳极氢氧化反应(HOR)仍依赖铂族金属(PGMs), 碱性环境下HOR动力学较酸性条件降低2–3个数量级, 迫使电极必须采用高PGMs负载以维持性能。尽管Pt基催化剂活性优异, 但其稀缺性、高成本及CO中毒风险严重制约了AEMFCs实际应用。钌(Ru)因成本低、

氢吸附自由能( $\Delta G_{H^*}$ )接近Pt, 被视为理想替代材料, 但单质Ru的强Ru–H键阻碍了HOR的Volmer步骤, 导致动力学迟滞. 为此, 研究聚焦于多尺度电子结构调控策略: 通过将Ru与低电负性3d过渡金属进行合金化促进电子转移, 优化d带中心以降低 $\Delta G_{H^*}$ ; 采用单原子修饰技术最大化原子利用率并提升本征活性; 结合杂原子掺杂改变载体电子分布增强催化稳定性. 这些协同策略通过优化氢( $H^*$ )与羟基( $OH^*$ )中间体的吸附强度, 为开发低成本、高效且耐CO的Ru基催化剂提供了新方向, 对推动AEMFCs商业化具有关键意义.

本文通过弱化学还原和氨辅助气相氮化制备方法, 将Cu/Ru双单原子和稀CuRu纳米合金整合在中空多孔碳载体上(N-(CuRu)<sub>NP+SA</sub>@NC), 设计并制造出了具有高活性和强抗CO中毒的Ru基HOR电催化剂. 其中N原子通过强烈的N-金属相互作用与Cu和Ru金属原子进行配位. 像差校正高角环形暗场扫描透射电子显微镜测试结果表明, 材料中同时存在孤立的Cu/Ru单原子和稀CuRu纳米合金颗粒. 光谱测试结果表明, N的掺杂致使Ru的电子云密度降低, 而Cu的电子云密度升高, 证实电子由Ru向Cu的定向转移. 这种电子重构有效优化了活性位点的吸附特性, 它使得Ru对H和CO的吸附能降低, 同时促使Cu对OH的吸附能升高, 从而在能量层面上为HOR反应的顺利推进创造了更有利的条件. 电化学测试结果表明, N-(CuRu)<sub>NP+SA</sub>@NC具有较高的交换电流密度和质量活性, 分别为3.74 mA cm<sup>-2</sup>和3.28 mA μg<sub>Ru</sub><sup>-1</sup>, 远远优于迄今为止报道的大多数Ru基催化剂. 在1000 ppm CO的高浓度环境中仍保持稳定活性, 展现出商用Pt/C无法企及的抗中毒能力. 密度泛函理论计算揭示, 合金化的稀CuRu合金纳米粒子和单分散Cu原子协同调控Ru的电子构型, 优化H/OH吸附并促进CO氧化, 从而提升碱性HOR活性和抗CO中毒能力. 系统实验和表征结果表明, N-(CuRu)<sub>NP+SA</sub>@NC较好的HOR性能可归因于以下4个因素: (1) N掺杂的多孔碳基质可有效缓解金属活性中心的溶解和团聚, 从而提高电催化剂的耐腐蚀性. (2) 连接的中空球体内外壁为电解质渗透和电子/离子转移提供了通道, 从而提高了催化活性和效率. (3) N的加入以及Cu元素调节了宿主Ru的电子结构, 从而削弱了H\*/CO\*的吸附, 增强了主要活性位点对OH\*的吸附, 从而显著提高了催化性能和抗CO能力. (4) HBE和OHBE对N-(CuRu)<sub>NP+SA</sub>@NC表面的协同效应极大地促进了Volmer步骤, 从而加速了碱性HOR过程.

综上所述, 本文采用合金化与单原子修饰的协同策略, 精确调控了N-(CuRu)<sub>NP+SA</sub>@NC催化剂活性位点与HOR关键中间体的相互作用机制, 成功突破碱性介质中HOR动力学的限制瓶颈, 为设计高效且耐CO中毒的PGMs替代催化剂提供了新范式, 推动AEMFCs商业化进程迈出关键一步.

**关键词:** 稀CuRu纳米合金; N掺杂; 氢氧化反应; 协同效应; CO耐受性

收稿日期: 2024-11-16. 接受日期: 2025-02-24. 上网时间: 2025-05-20.

\*通讯联系人. 电子信箱: xlyang@gxnu.edu.cn (杨秀林), qiujs@mail.buct.edu.cn (邱介山), bin.wu@ntu.edu.sg (武斌).

基金来源: 国家自然科学基金(52363028, 21965005); 广西自然科学基金(2021GXNSFAA076001); 广西科技基地与人才课题(GUIKE AD23023004, GUIKE AD20297039); 新加坡国家研究基金(U2305D4003).